Physics of Fluids

Numerical investigation of wake structures of an atmospheric entry capsule by modal analysis

Cite as: Phys. Fluids **31**, 074105 (2019); https://doi.org/10.1063/1.5092166
Submitted: 08 February 2019 • Accepted: 27 June 2019 • Published Online: 22 July 2019

Yuya Ohmichi, Kenji Kobayashi and Masahiro Kanazaki

Numerical investigation of wake structures of an atmospheric entry capsule by modal analysis

Cite as: Phys. Fluids 31, 074105 (2019); doi: 10.1063/1.5092166
Submitted: 8 February 2019 • Accepted: 27 June 2019 •
Published Online: 22 July 2019

Yuya Ohmichi,[1,a)] Kenji Kobayashi,[2] and Masahiro Kanazaki[2]

AFFILIATIONS

[1] Aeronautical Technology Directorate, Japan Aerospace Exploration Agency, 7-44-1 Jindaiji-Higashi, Chofu, Tokyo 182-8522, Japan
[2] Graduate School of System Design, Tokyo Metropolitan University, 6-6 Asahigaoka, Hino, Tokyo 191-0065, Japan

[a)] Electronic mail: ohmichi.yuya@jaxa.jp

ABSTRACT

This study investigates the flow structures behind an atmospheric entry capsule at Mach number 0.4 through an improved detached eddy simulation and a modal analysis. The simulated flowfields reveal relatively low-frequency peaks of $St \approx 0.016$ and $St = 0.17$–0.2 in the aerodynamic coefficient variation, where St is the nondimensional frequency. Then, the dominant fluid structures that cause the frequency peaks are identified through dynamic mode decomposition and the compressive-sensing-based mode selection method. Many of the dominant fluid phenomena have a frequency of $St \approx 0.2$. In this frequency range, the fluid phenomena are mainly characterized with a large-scale vortex shedding separated from the capsule's shoulder part and with a helical fluid structure in the wake. Moreover, the variation in the lift coefficient of the capsule is mainly attributed to the large-scale vortex shedding phenomenon. Furthermore, a fluid phenomenon at a frequency of $St = O(0.01)$ is found, which describes the pulsation, or periodic growth or shrinkage, of the recirculation bubble, accompanied by pressure fluctuation behind the capsule that exerts a large drag fluctuation of the capsule. Additionally, this phenomenon seems related to the dynamic instability phenomena of the capsule, as indicated by its time scale, which is close to that of the capsule's attitude motion.

I. INTRODUCTION

Atmospheric entry capsules tend to be dynamically unstable at a wide range of subsonic and supersonic speeds.[1–5] For example, the pitching angle of the capsule oscillates at a limit-cycle state, or its oscillation amplitude grows and finally diverges. As such properties largely relate to the success or failure of a mission, they should be designed to accurately predict the dynamic instability of the capsule, a phenomenon assumingly attributed to the near-wake fluid phenomenon of the bluff-body-shaped capsule. Teramoto and Fujii[6,7] investigated flowfields around the capsule under forced pitching oscillation, on a hypothetical basis that dynamic instability is a phase lag between the attitude motion of the capsule and a pressure fluctuation in the recirculation bubble behind the capsule, leading to hysteresis in pitching moment variation. Sammonds[8] and Chapman *et al.*[9] found both experimentally and numerically that transforming the flat aftbody of the capsule into a hemispherical shape made it more stable.

One of the causes of amplitude divergence in general oscillation is the resonance phenomenon, where the oscillation amplitude dramatically increases as the oscillator receives a periodic external force having a close-to-natural frequency. With respect to the dynamic instability of the atmospheric entry capsule, if the Strouhal number is defined as $St = fD/U_\infty$ using capsule diameter D, uniform flow velocity U_∞, and frequency f, then the typical oscillation frequency of the capsule observed in the experiment is $St = O(0.01)$.[2,3] Nevertheless, past studies on atmospheric entry capsules have not reported fluid phenomena at a frequency on the order of $St = O(0.01)$ although they have generally confirmed the vortex shedding phenomena of $St = O(0.1)$ and separated shear layer instability of $St = O(1.0)$.

Many studies have shown that the wake structure of a basic bluff body shape, such as spheres and thin disks, produces similar fluid structures. In particular, fluid phenomena having frequencies of the order of $St = O(0.01)$ have been confirmed in experiments and numerical simulations. Based on experimental observations, Berger *et al.*[10] proposed that low-frequency fluctuations occurring behind a disk and a sphere correspond to the pulsation motion of a recirculation bubble, which Yang *et al.*[11] validated via numerical simulations. Tian *et al.*[12] recently analyzed the variation in the recirculation bubble size behind a disk of Reynolds number $Re = 1.5 \times 10^5$ by large eddy simulation, which apparently showed a near-wake pressure fluctuation of $St = 0.01$ recirculation bubble pulsation. Moreover, the low-frequency oscillations were also found in the wake of two-dimensional cylinder bodies[13,14] and axisymmetric slender bodies.[15,16] Based on these results, the occurrence of a similar low-frequency phenomenon can be presumed in a capsule's wake.

To clarify the mechanism of the dynamic instability, the coupled analysis including the motions of the capsule and the flowfield around it is necessary. However, only a few studies have highlighted the unsteady behavior of the three-dimensional fluid structure of the wake even in the case of a stationary capsule. This study aims to clarify the three-dimensional spatial structure and its temporal behavior of the flowfield around a stationary capsule at subsonic speed. We initially perform an unsteady fluid simulation via improved delayed detached eddy simulation (IDDES).[17] Next, we employ dynamic mode decomposition (DMD)[18,19] to the unsteady flowfield data obtained around the capsule for extraction of the fluid phenomena contained in the wake. Furthermore, using a mode selection method based on compressive sensing,[20] we identify DMD modes representing particularly dominant fluid phenomena and clarify the fluctuation of aerodynamic forces (the lift, drag, lateral forces, and the pitching moment) these fluid phenomena give to the capsule.

II. FLUID SIMULATION

A. Test conditions

We used a capsule-shaped re-entry vehicle called the H-II transfer vehicle-return (HTV-R) vehicle[21] shown in Fig. 1, which had been planned by the Japan Aerospace Exploration Agency (JAXA), as the test model. Koga *et al.*[5] conducted a single-degree-of-freedom (1-DOF) free-rotation test on this model and found remarkable dynamic instability at Mach numbers of 0.4 and 1.1. We set Mach number to 0.4 to investigate the wake structures at subsonic speeds. The Reynolds number defined by the freestream velocity U_∞ and the capsule's maximum diameter D was $Re = 1.9 \times 10^6$. The angle of attack was fixed to $\alpha = 20^\circ$, which is the design trim angle of HTV-R.

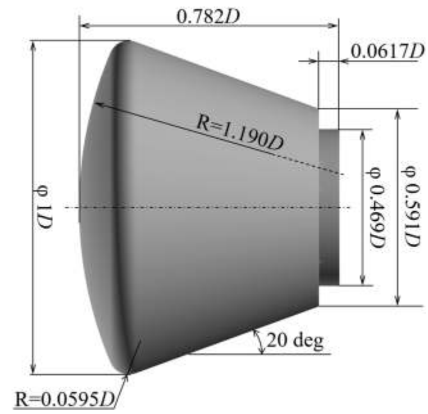

FIG. 1. Overview of the test model.

B. Flow solver

We performed a simulation using FaSTAR,[22] which is an unstructured numerical fluid simulation code developed by JAXA, governed by three-dimensional compressible Navier–Stokes equations. Inviscid flux and the gradient were evaluated using the Harten–Lax–van Leer–Einfeldt–Wada[23] scheme and the Green–Gauss least-squares method, respectively.[24] Second-order spatial accuracy was achieved using the monotonic upwind scheme for conservation law method.[25] We applied IDDES based on the Spalart-Allmaras turbulence model (SA-IDDES)[26] and performed time integration via the lower-upper symmetric Gauss–Seidel (LU-SGS) method.[27] Moreover, second-order temporal accuracy was achieved by solving the second-order backward differences using the dual-time stepping method,[28] for a time step size of $\Delta t_{\rm CFD} U_\infty / D = 1.40 \times 10^{-3}$. Hashimoto *et al.*[29] successfully reproduced the results of a wind tunnel experiment of HTV-R[5] through FaSTAR by following the stated calculation methods.

Figure 2 shows the computational mesh we used in the simulation. It was generated by the HexaGrid[30] software developed

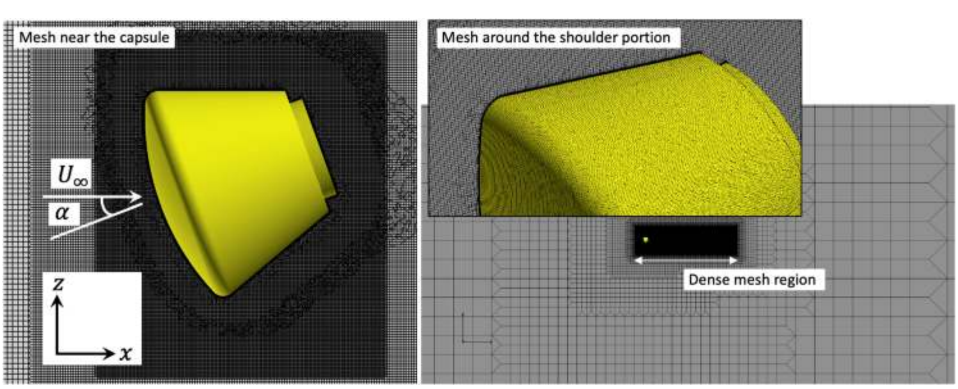

FIG. 2. Computational mesh.

by JAXA, which is capable of generating body-fitted layered meshes on no-slip walls and Cartesian meshes in the other regions. The minimum mesh spacing on the wall surface was $y^+ = 1$. To accurately capture the wake flow, we uniformly subdivided the wake region ($x/D < 15$). The total number of grid points n_{cell} was approximately 5.6×10^7. Adiabatic and no-slip wall conditions were adopted for the capsule's body boundary, while a uniform flow condition was adopted for the far-field boundaries ($x/D = \pm 100$, $y/D = \pm 100$, $z/D = \pm 100$).

Appendix A details the validation of the present numerical simulation results.

III. MODAL ANALYSIS

We analyzed the three-dimensional unsteady flowfield data obtained from the fluid simulation through the modal decomposition methods described below. The modal decompositions were performed using FBasis,[20,31] which is a modal analysis tool for fluid dynamics datasets developed by JAXA.

A. Input datasets

The input dataset was a three-dimensional spatial distribution of the flowfield at each time. Each snapshot represents a d-dimensional vector in which five variables of density (ρ), velocity (u, v, and w), and pressure (p) on each cell used for computational fluid dynamics are arranged as follows:

$$\psi_k = [\rho_1 \; u_1 \; v_1 \; w_1 \; p_1 \cdots \rho_{n_{\text{cell}}} \; u_{n_{\text{cell}}} \; v_{n_{\text{cell}}} \; w_{n_{\text{cell}}} \; p_{n_{\text{cell}}}]^T, \tag{1}$$

where the subscript k (=1, . . ., N) on the left-hand side of the equation corresponds to the time ($t_k = k\Delta t$) of each snapshot and the subscript on the right-hand side represents the cell number. The time interval between the snapshots was $\Delta t U_\infty / D = 0.28$. The number of snapshots was $N = 3500$, which includes about 10 cycles of the low frequency phenomenon assuming that its frequency is $St = 0.01$.

Herein, the inner product between the data is defined as[32]

$$\langle \psi_i, \psi_j \rangle = \int_V (\rho_i \rho_j + u_i u_j + v_i v_j + w_i w_j + p_i p_j) \mathrm{d}V, \tag{2}$$

where V and $\mathrm{d}V$ are the computational domain and volume elements for which the data are defined. By defining the inner product in the form of the volume integral, we could reduce the dependence of the inner product calculation on the computational mesh.

B. Low dimensionalization

The dataset obtained by the present three-dimensional unsteady fluid simulation contained considerable data; thus, due to computational memory size limit, conventional modal decomposition methods were hardly applicable to the dataset. We solved the difficulty by low dimensionalization of the input dataset through the incremental proper orthogonal decomposition (incremental POD).[20,33]

Here, POD bases were calculated as orthogonal bases $P_r \in \mathbb{R}^{d \times r}$ that minimize the following equation:

$$\text{minimize } J_1(P_r) = \| \Psi - P_r P_r^T \Psi \|_F^2, \tag{3}$$

where $\|\cdot\|_F$ and $\Psi = [\psi_1 \cdots \psi_N] \in \mathbb{R}^{d \times N}$ represent the Frobenius norm and the input dataset, respectively.

To solve Eq. (3), conventional POD algorithms[34] need to simultaneously store the entire input dataset Ψ in computational memory, whereas the incremental POD only sequentially processes them one-by-one, thereby preventing the stacking of data in the computational memory, given a large amount of input. Incremental POD has been widely explained by Arora *et al.*[33] and Ohmichi.[20]

Thus, we low-dimensionalized the input dataset Ψ using the POD bases P_r given by the incremental POD algorithm as

$$\tilde{\Psi} = P_r^T \Psi, \tag{4}$$

to obtain dataset $\tilde{\Psi} = [\tilde{\psi}_1 \cdots \tilde{\psi}_N] \in \mathbb{R}^{r \times N}$. In this study, we set $r = 81$. The contribution rate of POD modes is discussed in Appendix B.

C. Dynamic mode decomposition

DMD is a modal decomposition method developed by Schmid[18] that considers a linear operator A satisfying the relation

$$\Psi_1 \approx A \Psi_0, \tag{5}$$

where $\Psi_0 = [\psi_1 . . . \psi_{N-1}]$ and $\Psi_1 = [\psi_2 . . . \psi_N]$ denote partial matrices of the input datasets Ψ. The DMD mode is obtained as the eigenvalue λ and eigenvector ϕ of the eigenvalue problem

$$A\phi = \lambda \phi. \tag{6}$$

In other words, DMD approximates the time evolution of input variables with a linear system and expresses those data through the superposition of system solutions. Many methods have been proposed for the DMD algorithm; this study employed the total least squares DMD (TDMD) method[19] to obtain matrix A that satisfies Eq. (5) as it has better input dataset reproducibility performance compared to the conventional DMD algorithm employing the ordinary least squares method. This algorithm is detailed by Hemati *et al.*[19]

To handle the large dataset described above, we used low dimensional dataset $\tilde{\Psi}$ as the input dataset of DMD instead of Ψ. The DMD mode (λ, ϕ) of the original dataset Ψ was calculated from the DMD mode $(\tilde{\lambda}, \tilde{\phi})$ of $\tilde{\Psi}$ through

$$\lambda = \tilde{\lambda} \text{ and } \phi = P_r \tilde{\phi}. \tag{7}$$

The growth rate σ and oscillation frequency St of each corresponding DMD mode can be calculated from λ as follows:

$$\sigma = \frac{\log(|\lambda|)}{\Delta t} \text{ and } St = \frac{\mathrm{Arg}(\lambda)}{2\pi \Delta t}. \tag{8}$$

D. Identification of dominant modes

One drawback of DMD is identifying which among the obtained modes is physically important. This is solved by the compressive sensing approach introduced by Jovanović *et al.*[35] using the least absolute shrinkage and selection operator (LASSO).[36] With this technique, all input datasets are expressed in as few modes as possible while maintaining a small reconstruction error. Recently, a greedy compressive sensing method for DMD was proposed by Ohmichi,[20,31] as described next.

Referring to Alenius,[37] we defined the reconstruction formula for a criterion of mode selection as

$$\tilde{\Psi} \approx \tilde{\Phi} C, \tag{9}$$

$$= \begin{bmatrix} \tilde{\phi}_1 & \cdots & \tilde{\phi}_r \end{bmatrix} \begin{bmatrix} c_{11} & \cdots & c_{1N} \\ \vdots & \ddots & \vdots \\ c_{r1} & \cdots & c_{rN} \end{bmatrix}. \tag{10}$$

That is, the coefficient $c_k = [c_{1k} \cdots c_{rk}]^T$ is determined for each time step $k = 1, \ldots, N$. The optimal coefficient is obtained by $C_{\mathrm{opt}} = \tilde{\Phi}^{+}\tilde{\Psi}$ through $\tilde{\Phi}^{+}$, which is the pseudoinverse matrix of $\tilde{\Phi}$. From these formulas, we found important modes that are a combination of modes minimizing the reconstruction error as

$$\text{minimize } J_2(\mathcal{S}) = \|\tilde{\Psi} - \tilde{\Phi}_{\mathcal{S}}\tilde{\Phi}_{\mathcal{S}}^{+}\tilde{\Psi}\|_F^2, \tag{11}$$

where $\mathcal{S} = \{j | j \in \{1, \ldots, r\}, \tilde{\phi}_j \neq 0\}$ is a subscript set, $\tilde{\Phi}_{\mathcal{S}}$ is a matrix obtained by replacing the DMD mode corresponding to the subscript not included in the subscript set $\mathcal{S}$ by 0 for the matrix $\tilde{\Phi} = [\tilde{\phi}_1 \cdots \tilde{\phi}_r]$; that is, $\mathcal{S}$ represents a combination of selected DMD modes.

Moreover, we used a compressive sensing algorithm based on the greedy method[20,31] to find the optimal set $\mathcal{S}$ that minimizes Eq. (11). In general, finding the exact solution of combinatorial optimization problems is a difficult task due to the very large computational complexity. The greedy algorithm is one of the most fundamental algorithms for obtaining approximate solutions of combinatorial optimization problems. Furthermore, it is known to provide a good approximate solution for several practical problems[38] at a low computational cost.

The greedy algorithm repeatedly selects a single mode for minimizing $J_2(\mathcal{S})$ in succession. In the initial iteration step, we obtain a mode that minimizes $J_2(\mathcal{S})$ for a single DMD mode by calculating the minimum reconstruction error $J_2(\mathcal{S})$ for each mode. In the next iteration step, we obtain a mode for a minimum $J_2(\mathcal{S})$ after combining it with the mode found from the initial step and then adding it to the set $\mathcal{S}$ as the second selection mode. In the subsequent iteration steps, the modes are selected in the same manner of succession. Iteration terminates after the number of selected modes reaches K (specified by the user). Through this pattern, the number of computations of the reconstruction error $J_2(\mathcal{S})$ becomes dramatically smaller than that yielded when all combinations are considered; thus, an approximate solution is obtained considering the practical computational cost. This algorithm is summarized in Algorithm 1. With the

ALGORITHM 1. Greedy mode selection algorithm.

Input: $\tilde{\Phi}, \tilde{\Psi}$, and sparsity level K.

Initialize: iteration counter $i = 0$, estimated support $\mathcal{S}^0 = \emptyset$.

while $i < K$ do
  $j_0 = \mathrm{argmin}_j J_2(\mathcal{S}^i \cup j), j \notin \mathcal{S}^i$,
  $\mathcal{S}^{i+1} = \mathcal{S}^i \cup j_0$,
  $i = i + 1$.
end

selected DMD mode, the reconstructed (approximate) dataset Ψ_R of the original input dataset Ψ can be calculated as

$$\Psi_R = P_r \tilde{\Phi}_{\mathcal{S}} \Phi_{\mathcal{S}}^{+} \tilde{\Psi}. \tag{12}$$

IV. RESULTS AND DISCUSSION

A. Fluid simulation results

Figure 3 shows the instantaneous flowfield obtained by IDDES. The vortex structure of the capsule's wake is visualized by the isosurface of the Q-value.[39] Flow separation at the capsule shoulder part is rapidly destabilized, with many generated small vortex structures. Moreover, a regular waviness structure appears in the wake on both x–y and x–z planes, as depicted in Fig. 3, suggesting the existence of a large-scale periodic vortex shedding phenomenon. Figure 4 shows the streamline of the time-averaged flowfield, which displays flow separation on the shoulder portion of the capsule as a result of its relatively sharp edge. As observed, a large recirculation region is generated behind the capsule, $0 < x/D < 2$.

Figure 5 shows a frequency distribution calculated from time-series data of lift, drag, and pitching moment coefficients. Power spectrum densities (PSDs) were calculated using Welch's method,[40] dividing the time-series data into five segments (with 50% overlap), resulting in frequency resolution $\Delta St = 2.7 \times 10^{-3}$. In the lift coefficient, a frequency peak of $St = 0.17$–0.2 is observed, which is due to the periodic vortex shedding mentioned above, and is coincident with the characteristic frequencies of wake instability of a sphere.[41,42] In the drag coefficient, $St \approx 0.016$ is dominant and the variation due to a vortex shedding of $St = 0.17$–0.2 is small, a similar tendency presumed to be observed in flowfields around a sphere.[43] Interestingly, this low frequency matches that of the dynamic instability phenomenon of the capsule observed in the experiment.[5] In the rest of this section, DMD and mode selection analysis are used to identify structures corresponding to these fluid phenomena.

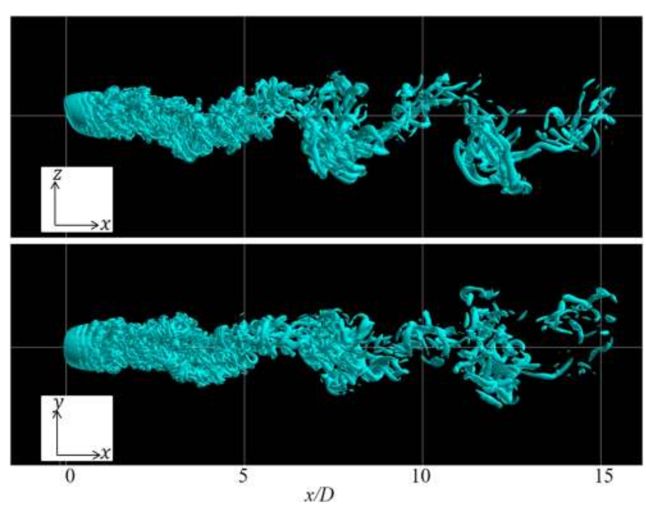

FIG. 3. Instantaneous flowfield obtained by IDDES. Vortex structures in the wake are illustrated with isosurfaces of Q-value.

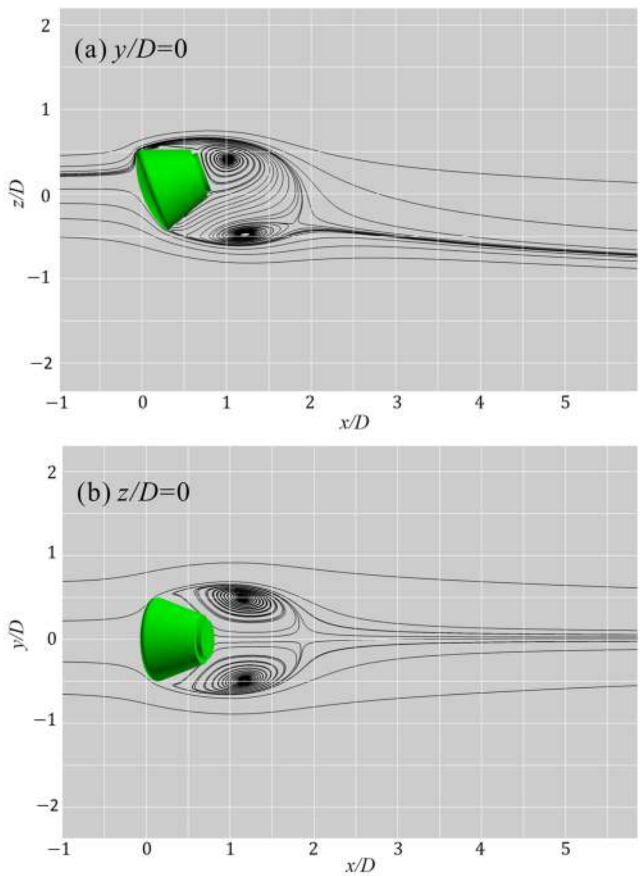

FIG. 4. Streamlines of the time-averaged flowfield at (a) $y/D = 0$ and (b) $z/D = 0$.

B. Eigenvalues and identified dominant modes

Figure 6 shows the eigenvalue distribution of each DMD mode, as well as the 11 modes specified as the dominant modes by the mode selection method described in Sec. II. (Here, because the oscillatory mode always appears as a pair of complex conjugate

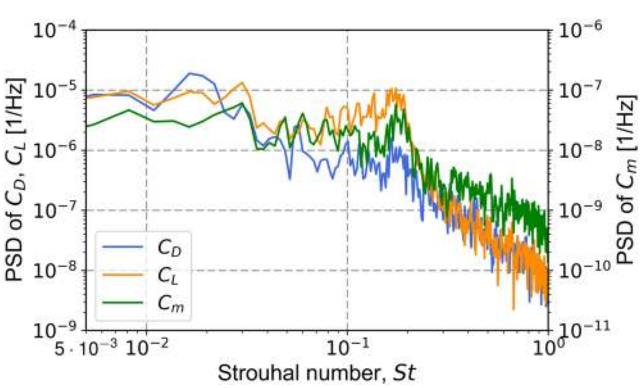

FIG. 5. Frequency distribution of lift, drag, and pitching moment coefficients.

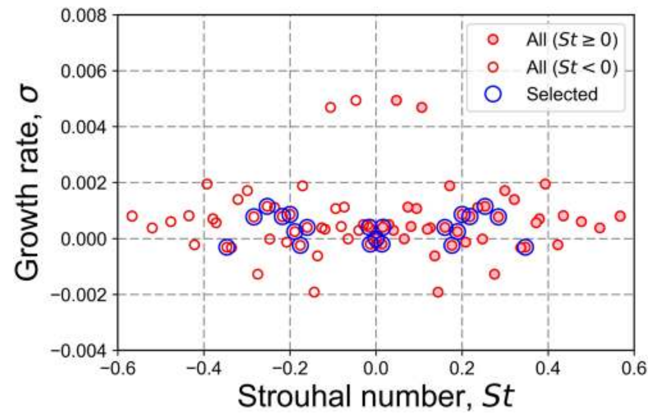

FIG. 6. Distributions of DMD eigenvalues and dominant modes identified by the mode selection algorithm. Note that negative frequency modes ($St < 0$) are complex conjugate modes of positive frequency modes.

modes, we count two modes of a pair as one mode.) First, the algorithm selects a mode where both growth rate and Strouhal number are 0, or a mode representing the mean flowfield. As for the other modes, those with frequencies near $St \approx 0.2$ are chosen mainly as the dominant modes. Furthermore, we confirm that the modes of $St = 0.0136$ and $St = 0.0159$, with frequencies smaller than these modes by one order of magnitude, are also dominant. Additionally, these frequencies are close to the frequency peak of the drag coefficient (Fig. 5) and coincident with the dynamic instability frequency observed in previous studies[3,5] and thus are expected to be related to the phenomenon. The characteristics of these dominant DMD modes are examined in detail in the subsequent texts.

C. Spatial structures of dominant modes

After examining the dominant modes specified by the mode selection algorithm, we reveal the existence of their characteristic spatial structures, as illustrated in Figs. 7–12. Figure 7 (Multimedia view) shows the DMD mode with $St = 0.189$. The isosurface of the freestream direction velocity component [Fig. 7(a), (Multimedia view)] shows large-scale vortex structures regularly shed from the top and bottom shoulder parts (namely, $+z$ and $-z$ sides) of the capsule. Figure 9 (Multimedia view) shows the mode of $St = 0.200$, whose spatial structure is similar to that of the mode of $St = 0.189$, but whose vortices are emitted from the left and right shoulder parts (namely, $+y$ and $-y$ sides) of the capsule, as also apparently observed from the distribution on the $z/D = 0$ plane [Fig. 9(c)]. Such staggered distribution appears in the modal analysis of Karman vortex streets, which expresses an advection phenomenon of regularly generated vortices from the left and right parts of the capsule. Presumably, the limited symmetry due to an angle of attack (nonaxisymmetric but symmetric with respect to the plane $y/D = 0$) caused the directional (top/bottom and left/right) vortex shedding phenomena, which is a difference between wakes of axisymmetric bodies (e.g., a sphere and a circular disk) and the capsule with an angle of attack. Marquet and Larsson[44] reported similar top/bottom and left/right vortex shedding instabilities behind rectangular plates by global

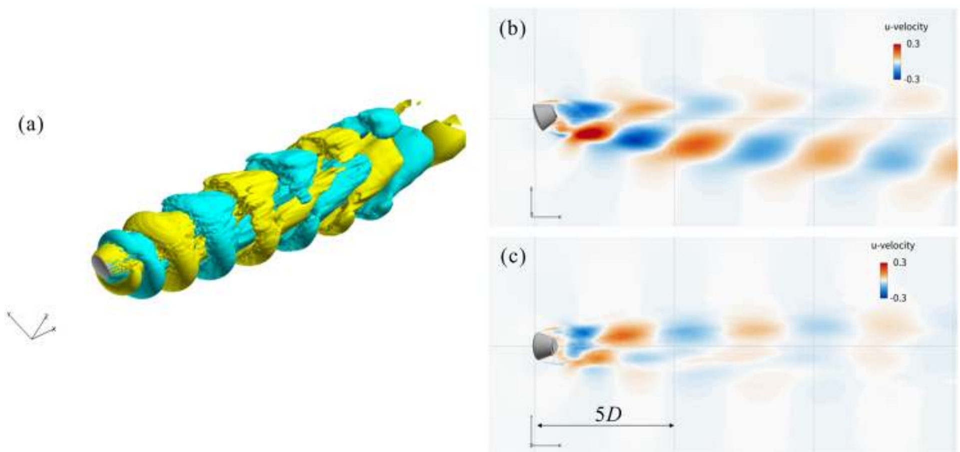

FIG. 7. Spatial structures of *St* = 0.189 mode. Velocity fluctuation component in the *x*-direction. (a) Isosurfaces (Multimedia view). Yellow and light blue indicate opposite signs. Distributions of the planes of (b) *y*/*D* = 0 and (c) *z*/*D* = 0. Multimedia view of (a): https://doi.org/10.1063/1.5092166.1

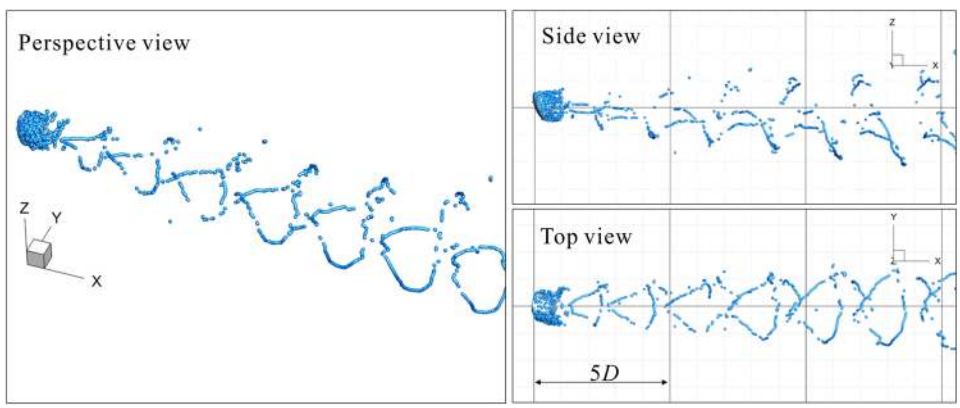

FIG. 8. Vortex cores of *St* = 0.189 mode indicated by blue plots.

stability analysis. Figures 8 and 10 show the vortex cores of the large-scale vortices. The vortex cores were identified by a method based on critical point theory.[45] The figures suggest that shapes of the vortices are hairpinlike vortex loops. Figure 11 (Multimedia view) gives the mode of $St = 0.176$, depicting a helical spatial structure generated from the capsule's shoulder part presumed to be caused by the rotation of a fluctuation phase in the capsule shoulder part in the circumferential direction. Similar helical structures are observed in the wake of a sphere and a disk by an experiment[10] and a numerical simulation.[42,46] Constantinescu and Squires[42] reported that the helical structures appear behind a sphere at low Reynolds numbers but disappear at high Reynolds numbers ($Re = 1.14 \times 10^6$ in their

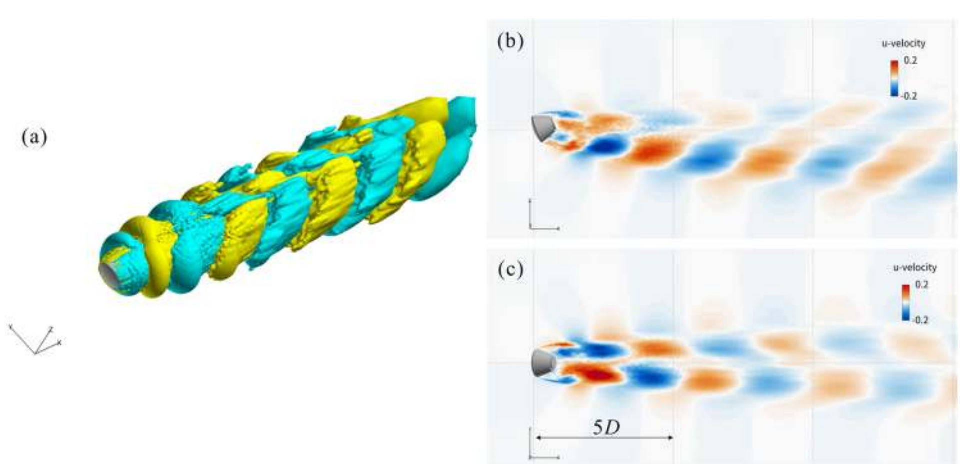

FIG. 9. Spatial structures of *St* = 0.200 mode. Velocity fluctuation component in the *x*-direction. (a) Isosurfaces (Multimedia view). Yellow and light blue indicate opposite signs. Distributions of the planes of (b) *y*/*D* = 0 and (c) *z*/*D* = 0. Multimedia view of (a): https://doi.org/10.1063/1.5092166.2

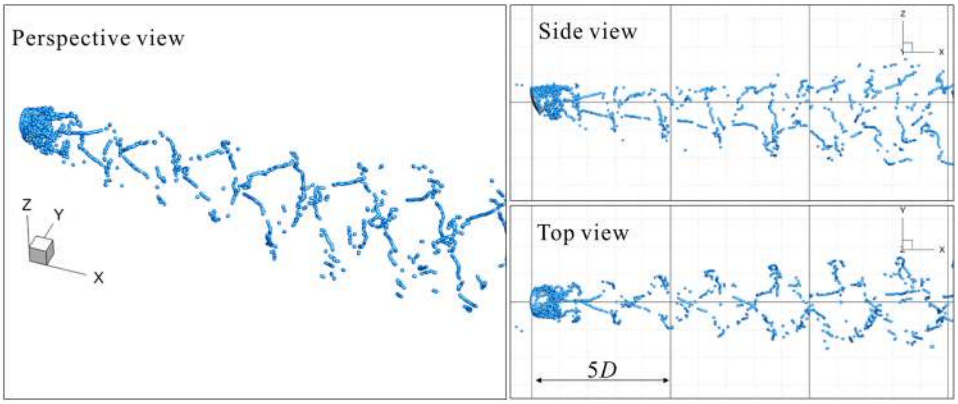

FIG. 10. Vortex cores of *St* = 0.200 mode indicated by blue plots.

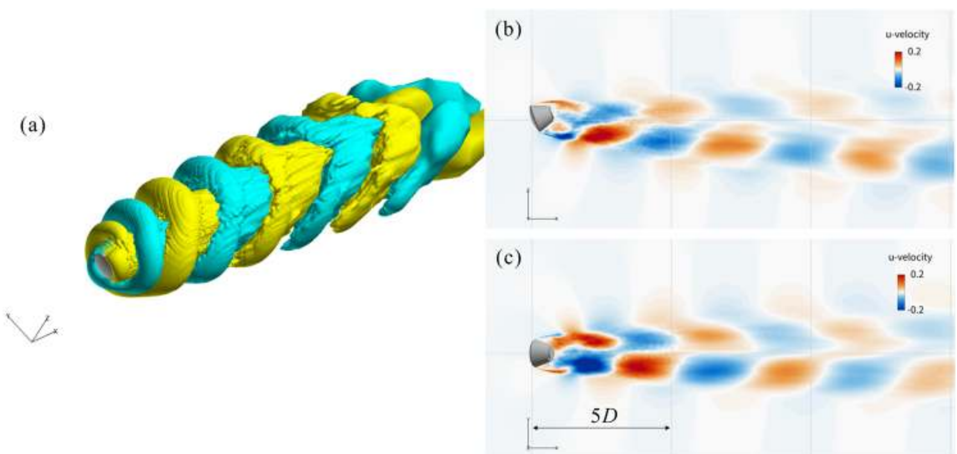

FIG. 11. Spatial structures of *St* = 0.176 mode. Velocity fluctuation component in the *x*-direction. (a) Isosurfaces (Multimedia view). Yellow and light blue indicate opposite signs. Distributions of the planes of (b) *y/D* = 0 and (c) *z/D* = 0. Multimedia view of (a): https://doi.org/10.1063/1.5092166.3

case). Berger *et al.*[10] reported that the wake structure of a circular disk is almost Reynolds-number-independent, whereas that of the sphere is not. It can be inferred that wake structures of an atmospheric entry capsule are similar to that of a circular disk since the capsule's shoulder portion has a relatively sharp edge. In summary, the fluid phenomenon having a frequency of *St* ≈ 0.2 can be described mainly by three types of dominant fluid structures, namely, large-scale vortex shedding separated from the top and bottom parts of the capsule's shoulder and from the left and right parts, and a helical fluid structure.

Figure 12 (Multimedia view) shows the mode of *St* = 0.0159. The spatial structure of this mode is significantly different from that

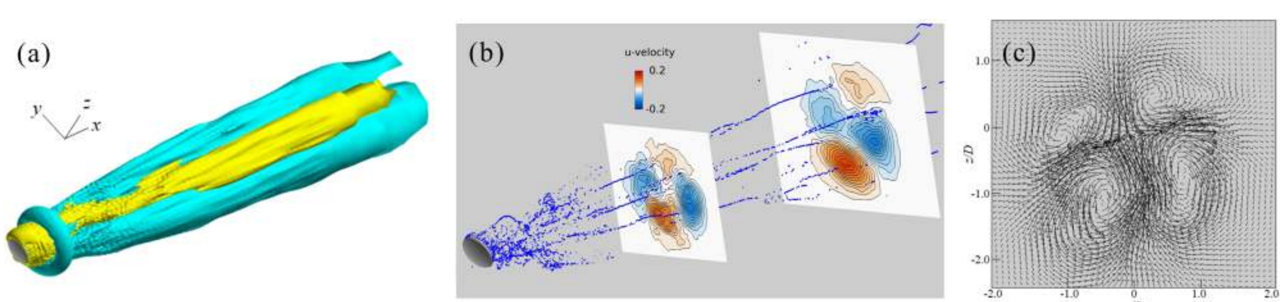

FIG. 12. Spatial structures of *St* = 0.0159 mode. Velocity fluctuation component in the *x*-direction. Same color scheme as in Fig. 7. (a) Isosurfaces (Multimedia view). (b) Distributions on the planes of *x/D* = 7.5 and 15, and vortex cores (indicated by blue lines). (c) Velocity vector field on the plane of *x/D* = 7.5. Multimedia view of (a): https://doi.org/10.1063/1.5092166.4

of the mode with $St \approx 0.2$ frequency. From Figs. 12(b) and 12(c), this mode shows longitudinal vortex structures downstream of the recirculation bubble behind the capsule. An animation of the figure (Multimedia view) confirms the slow motion of the vortices in the circumferential direction. Additionally, a pulsation motion of the velocity is observed at the near-wake of the capsule. A detailed motion of this phenomenon is provided in Sec. IV E.

D. Aerodynamic forces caused by each DMD mode

We clarify the influence of the fluid phenomenon caught as the dominant DMD mode on the aerodynamic coefficients. The contribution of each mode on the aerodynamic force is quantitatively evaluated via the rms amplitudes of the variation in the aerodynamic coefficient caused by each mode, as shown in Fig. 13. As expected from the frequency characteristics shown in Fig. 5, the low-frequency modes of $St = 0.0136$ and $St = 0.0159$ cause a large variation in the drag coefficient, while the modes of $St \approx 0.2$ cause a large variation in the lift and pitching moment coefficients. The aerodynamic force exerted by modes with relatively high frequencies ($St = 0.253$, 0.284, 0.347) is small.

After an in-depth observation, we understand the correspondence between the spatial structure of each mode and the aerodynamic force each exerts on the capsule. As such, the mode of $St = 0.189$, which represents vortex shedding from the capsule's top and bottom shoulders, as shown in Fig. 7 (Multimedia view), has the most significant influence on the lift and pitching moment variations. Similarly, the mode of $St = 0.200$, which represents vortex shedding from the capsule's right and left shoulders, has a large contribution to the lateral force variation. Furthermore, the mode of $St = 0.176$, representing the helical structure in the wake, has an almost comparable contribution as the lift and lateral force variations. Interestingly, the mode of $St = 0.0136$ and $St = 0.0159$ dominates the contribution to the drag force variation and has a contribution to lift, lateral, and pitching moment variations, thereby indicating its significant influence on the unsteady aerodynamic characteristics of the capsule.

E. Near-wake structure of $St = O(0.01)$ modes

The DMD modes of $St = 0.0136$ and $St = 0.0159$ had a time scale comparable to that of the low-frequency fluid phenomenon[10,12] confirmed in the near-wakes of a circular disk and a sphere. Figure 14 (Multimedia view) shows the streamline and pressure fluctuation distributions of $St = 0.0159$ mode. Notably, the pressure fluctuation around the capsule is important from the viewpoint of an unsteady aerodynamic force on the capsule. In the figure, the flowfield is the superposition of the mean flowfield $\bar{x}$ and the mode ϕ of $St = 0.0159$ obtained by the equation

$$x(\theta) = \bar{x} + C_0(\phi_R \cos\theta - \phi_I \sin\theta), \tag{13}$$

where ϕ_R and ϕ_I are the real and imaginary parts of the present DMD mode ϕ, respectively; θ represents the phase; and C_0 is the amplitude set herein as the moment at which the drag fluctuation due to this mode is maximum.

As observed, the length of the recirculation bubble behind the capsule periodically changes (this fact can be more easily understood through the animation), a pulsation motion similar to that observed in the flowfield behind a circular disk by Berger *et al.*[10] and Tian *et al.*[12] Moreover, this pulsation motion is apparently accompanied by periodic pressure fluctuations in the recirculation bubble: bubble size varies in the presence of pressure gradient. The drag force acting on the capsule correspondingly decreases with bubble growth and increases with bubble shrinkage. The peaks of pressure fluctuation occur near separation lines as indicated in the figure, which is consistent with the observations by Berger *et al.*[10] The fluid structure of $St = 0.0136$ mode (not shown here) is similar to that of the $St = 0.0159$ mode, with the presence of a little asymmetry in the former, which results in a lateral force (Fig. 13).

As mentioned above, the time scale of the pulsation motion is close to the typical time scale of the capsule attitude motion [$St = O(0.01)$, which is determined by the dynamic pressure of uniform flow and moment of inertia of the capsule]. In addition, the pulsation motion is accompanied by a pitching moment oscillation, as shown in Fig. 13. The facts suggest the mechanism by which this pulsation phenomenon acts on the attitude motion of the capsule and causes excitation of the oscillation of the capsule due to the resonance phenomenon although further investigations are needed to prove this hypothesis. Moreover, it suggests paying attention to the influence of support-sting on unsteadiness of the recirculation bubble as the dynamic instability of a bluff body-shaped capsule is examined via a wind tunnel test.

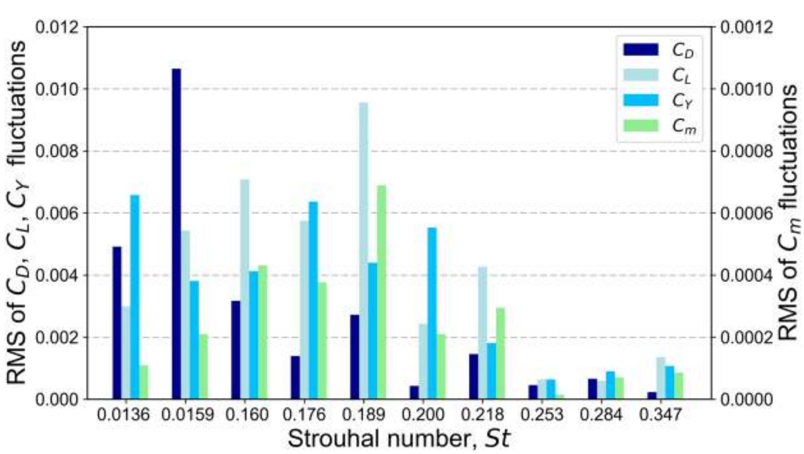

FIG. 13. Root-mean-square (rms) amplitude of the aerodynamic coefficient fluctuation that each DMD mode exerts on the capsule.

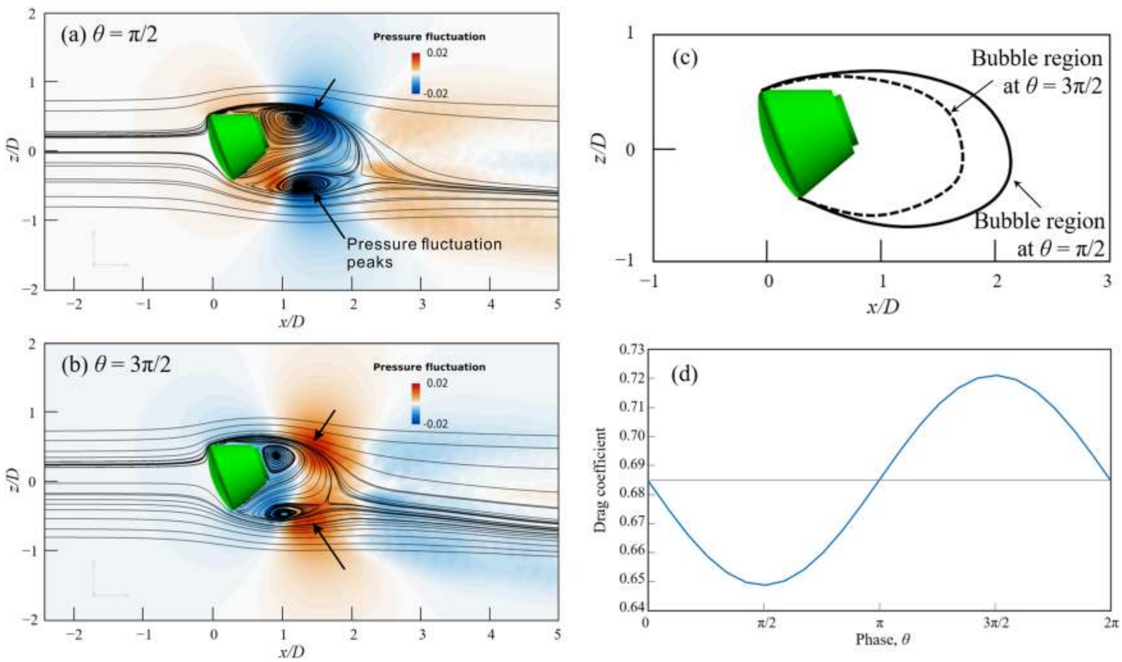

FIG. 14. Temporal change in the recirculation bubble in $St = 0.0159$ mode. Streamline and amplitude distributions of pressure fluctuation at $y/D = 0$ at phases (a) $\theta = \pi/2$ and (b) $\theta = 3\pi/2$ (Multimedia view). (c) Maximum and minimum bubble size. (d) Drag coefficient as a function of phase θ. Multimedia view of (b): https://doi.org/10.1063/1.5092166.5

V. CONCLUSION

This study employs IDDES and modal analysis to investigate coherent structures in the wake of an atmospheric entry capsule at subsonic speed. The results of IDDES revealed two peak frequencies at $St = 0.17$–0.2 and $St = 0.016$ in the fluctuations of lift and drag coefficients, respectively. For the modal analysis, DMD and mode selection algorithms for large datasets were used. The flow-field data obtained by IDDES were decomposed into DMD modes, the dominant of which were identified by the selection method. This modal analysis enabled us to clarify the three-dimensional spatial structures of the dominant fluid phenomena, their unsteady behaviors, and aerodynamic forces these phenomena give to the capsule.

Modal analysis results showed the three-dimensional spatial structures of the dominant fluid phenomena of $St \approx 0.2$ and $St = O(0.01)$. The DMD modes of $St \approx 0.2$ represented large-scale vortex shedding phenomena and a helical fluid structure, while the low-frequency DMD mode of $St = O(0.01)$ represented the pulsation phenomenon of a recirculation bubble (characterized by periodic changes in bubble size) and longitudinal vortices behind it.

Furthermore, the contribution of these fluid phenomena on the aerodynamic coefficient fluctuations of the capsule was clarified. The results confirmed that the lift and drag coefficient fluctuations were dominated by large-scale vortex shedding phenomena (of $St \approx 0.2$) and pulsation of the recirculation bubble [of $St = O(0.01)$], respectively. The latter phenomenon of $St = O(0.01)$ has not been reported yet in the literature of atmospheric entry capsules research but seems to be a similar phenomenon described in previous studies on the wake of a circular disk and a sphere;[10] moreover, its frequency is close to the typical oscillation frequency of the dynamic instability of capsules. Therefore, its coupling with the attitude motion of the capsule may cause excitation of the capsule's oscillation amplitude due to the resonance phenomenon. To clarify the excitation mechanism, the coupled analysis of the attitude motion and flow around the capsule is necessary and will be conducted in future works.

ACKNOWLEDGMENTS

The authors appreciate technical support provided by Kenji Hayashi of Ryoyu Systems Co., Ltd. This work was supported in part by the Japan Society for the Promotion of Science (JSPS) KAKENHI (Grant No. JP16H01563). The numerical computations were performed on the JAXA Supercomputer System 2 (JSS2).

APPENDIX A: VALIDATION OF SIMULATION RESULTS

To validate the present simulation results, we conducted fluid simulations with three different meshes and time step sizes

TABLE I. Number of cells and time step sizes for three simulations of grid dependency.

Label	Number of cells	Time step size ($\Delta t_{CFD} U_\infty / D$)
Coarse	9.6×10^6	6.8×10^{-3}
Baseline	2.4×10^7	3.4×10^{-3}
Fine	5.6×10^7	1.4×10^{-3}

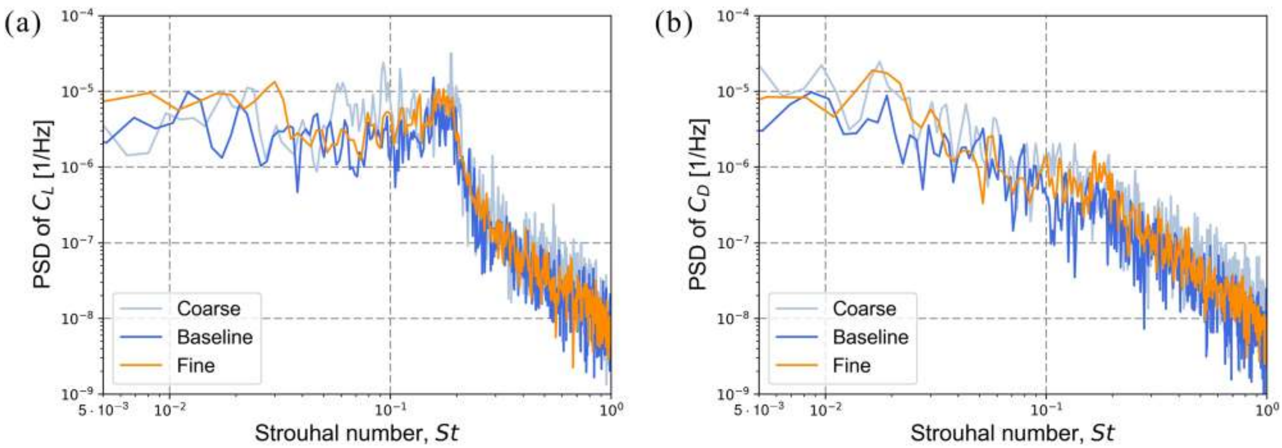

FIG. 15. Frequency distributions of (a) lift and (b) drag coefficients obtained with three simulations of grid dependency.

TABLE II. Dominant DMD modes for three simulations.

Label	Strouhal number of dominant DMD modes										
Coarse	0,	±0.00436,	±0.0129,	±0.0496,	±0.153,	±0.176,	±0.186,	±0.205,	±0.212,	±0.263,	±0.300
Baseline	0,	±0.0196,	±0.0352,	±0.159,	±0.180,	±0.189,	±0.209,	±0.227,	±0.243,	±0.291,	±0.337
Fine	0,	±0.0136,	±0.0159,	±0.160,	±0.176,	±0.189,	±0.200,	±0.218,	±0.253,	±0.284,	±0.347

summarized in Table I for investigating the grid dependency of the flow characteristics obtained by the present numerical simulation and compared the simulated results with experimental results.

Figure 15 shows the frequency distribution of lift and drag coefficients obtained with the three meshes, and Table II shows the list of 11 dominant DMD modes obtained by DMD and mode selection method detailed in Sec. III. Note that we cannot expect the exact matches between the mode frequencies of different simulations because the fluid phenomena are not completely periodic and the input signal has a finite length. Nevertheless, both the figure and table qualitatively validated similar frequency characteristics for the three results, that is, the presence of dominant fluid phenomena of $St = O(0.01)$ and $St \approx 0.2$, corresponding to an unsteady recirculation region and large-scale vortex sheddings, respectively.

TABLE III. Mean drag and lift coefficients of numerical simulations and wind tunnel experiments. The experimental results are taken from the work of Mitsuo *et al.*[47]

Label	C_D	C_L
Present simulation		
Coarse mesh	0.680	0.241
Baseline mesh	0.668	0.246
Fine mesh	0.690	0.262
Experiment ($M = 0.4$)		
$Re = 1.65 \times 10^6$	0.68	0.27
$Re = 1.98 \times 10^6$ with dots	0.57	0.34

Table III lists the time averaged values of the drag and lift coefficients of the present numerical and previous experimental results.[47] The table shows that the numerical results obtained with the fine mesh approximately reproduced the experimental results of $Re = 1.65 \times 10^6$. Note that, in the experiment of $Re = 1.98 \times 10^6$, surface roughnesses (dots) were applied on the capsule surface and it led to large difference from other cases. Although flowfields are not shown in Mitsuo *et al.*,[47] it is presumed that this difference was due to the change in separation locations. In the present simulation, the flow largely separates at the capsule's shoulder (shown in Fig. 4), and the flowfield around the capsule without the surface roughness is reproduced as a result.

The numerical result obtained with the fine mesh was analyzed in this study.

APPENDIX B: CONTRIBUTION RATE OF POD MODES

Figure 16 plots the contribution rate of each POD mode obtained by incremental POD with $r = 81$. The contribution rate is the eigenvalue of POD so that the sum of eigenvalues of all modes excluding the mean mode is unity and represents the percentage of variance for each POD mode. This figure shows that a relatively small number of modes account for a large proportion of the flowfield variation. The first 14 modes account for about 50% of the flowfield variation, and the 28th and subsequent modes have only 1% or less of the variation. This result enhances confidence in the validity of reducing the dimensionality of the input datasets using the POD modes.

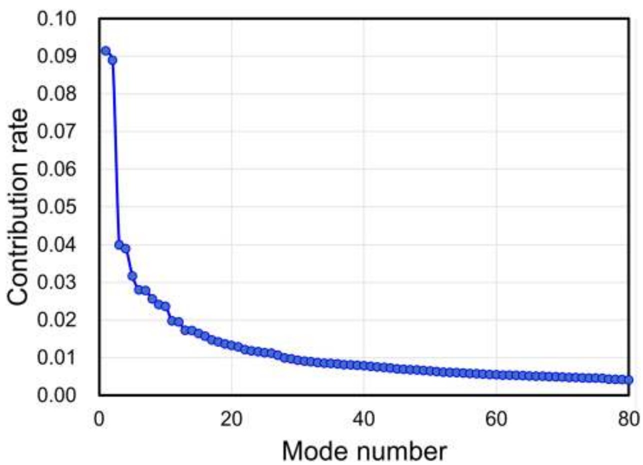

FIG. 16. Contribution rate of POD modes. Note that the mean mode (zeroth mode) is omitted.

REFERENCES

[1] L. E. Ericsson and J. P. Reding, "Re-entry capsule dynamics," J. Spacecr. Rockets **8**, 579–586 (1971).

[2] C. D. Kazemba, R. D. Braun, I. G. Clark, and M. Schoeneberger, "Survey of blunt-body supersonic dynamic stability," J. Spacecr. Rockets **54**, 109 (2017).

[3] K. Hiraki, Y. Inatani, N. Ishii, T. Nakajima, and M. Hinada, "Dynamic stability of MUSES-C capsule," in *21st International Symposium on Space Technology and Science* (21st ISTS Publication Committee, 1998), pp. ISTS 98–d–83.

[4] T. Ohashi, Y. Takahashi, H. Terashima, and N. Oshima, "Aerodynamic instability of flare-type membrane inflatable vehicle in suborbital reentry demonstration," J. Fluid Sci. Technol. **13**, JFST0020 (2018).

[5] S. Koga, A. Hidaka, R. Tagai, T. Kimura, T. Yoshinaga, and S. Nagai, "Dynamic stability testing of a reentry lifting capsule in a transonic wind tunnel," AIAA Paper 2014-1119, 2014.

[6] S. Teramoto and K. Fujii, "Numerical analysis of dynamic stability of a reentry capsule at transonic speeds," AIAA J. **39**, 646–653 (2001).

[7] S. Teramoto and K. Fujii, "Mechanism of dynamic instability of a reentry capsule at transonic speeds," AIAA J. **40**, 2467–2475 (2002).

[8] R. Sammonds, "Transonic static- and dynamic-stability characteristics of two large-angle spherically blunted high-drag cones," AIAA Paper No. 70-564, 1970.

[9] G. Chapman, C. Berner, G. Winchenbach, W. Hathaway, and R. Mitcheltree, "The use of spherical bases to eliminate limit cycles of blunt entry vehicles," AIAA Paper No. 99-1023, 1999.

[10] E. Berger, D. Scholz, and M. Schumm, "Coherent vortex structures in the wake of a sphere and a circular disk at rest and under forced vibrations," J. Fluids Struct. **4**, 231–257 (1990).

[11] J. Yang, M. Liu, G. Wu, Q. Liu, and X. Zhang, "Low-frequency characteristics in the wake of a circular disk," Phys. Fluids **27**, 064101 (2015).

[12] X. Tian, M. C. Ong, J. Yang, and D. Myrhaug, "Large-eddy simulations of flow normal to a circular disk at $Re = 1.5 \times 10^5$," Comput. Fluids **140**, 422–434 (2016).

[13] J. J. Miau, J. T. Wang, J. H. Chou, and C. Y. Wei, "Characteristics of low-frequency variations embedded in vortex-shedding process," J. Fluids Struct. **13**, 339–359 (1999).

[14] O. Lehmkuhl, I. Rodriguez, R. Borrell, and A. Oliva, "Low-frequency unsteadiness in the vortex formation region of a circular cylinder," Phys. Fluids **25**, 085109 (2013).

[15] V. Gentile, F. F. J. Schrijer, B. W. Van Oudheusden, and F. Scarano, "Low-frequency behavior of the turbulent axisymmetric near-wake," Phys. Fluids **28**, 065102 (2016).

[16] G. Pavia, M. Varney, M. Passmore, and M. Almond, "Three dimensional structure of the unsteady wake of an axisymmetric body," Phys. Fluids **31**, 025113 (2019).

[17] M. L. Shur, P. R. Spalart, M. K. Strelets, and A. K. Travin, "A hybrid RANS-LES approach with delayed-DES and wall-modelled LES capabilities," Int. J. Heat Fluid Flow **29**, 1638–1649 (2008).

[18] P. J. Schmid, "Dynamic mode decomposition of numerical and experimental data," J. Fluid Mech. **656**, 5–28 (2010).

[19] M. S. Hemati, C. W. Rowley, E. A. Deem, and L. N. Cattafesta, "De-biasing the dynamic mode decomposition for applied Koopman spectral analysis of noisy datasets," Theor. Comput. Fluid Dyn. **31**, 349–368 (2017).

[20] Y. Ohmichi, "Preconditioned dynamic mode decomposition and mode selection algorithms for large datasets using incremental proper orthogonal decomposition," AIP Adv. **7**, 075318, 1704.03181 (2017); e-print arXiv:1704.03181.

[21] Y. Suzuki and T. Imada, "Concept and technology of HTV-R: An advanced type of H-II transfer vehicle," Trans. Jpn. Soc. Aeronaut. Space Sci. Aerosp. Technol. Jpn. **10**, 9–18 (2012).

[22] A. Hashimoto, K. Murakami, and T. Aoyama, "Toward the fastest unstructured CFD code'FaSTAR'," AIAA Paper 2012-1075, 2012.

[23] S. Obayashi and G. P. Guruswamy, "Convergence acceleration of a Navier-Stokes solver for efficient static aeroelastic computations," AIAA J. **33**, 1134–1141 (1995).

[24] E. Shima, K. Kitamura, and K. Fujimoto, "New gradient calculation method for MUSCL type CFD schemes in arbitrary polyhedra," AIAA Paper 2010-1081, 2010.

[25] C. Burg, "Higher order variable extrapolation for unstructured finite volume RANS flow solvers," AIAA Paper 2005-4999, 2005.

[26] P. R. Spalart and S. R. Allmaras, "A one-equation turbulence model for aerodynamic flows," AIAA Paper 92-0439 (1992).

[27] D. Sharov and K. Nakahashi, "Reordering of hybrid unstructured grids for lower-upper symmetric Gauss-Seidel computations," AIAA J. **36**, 484–486 (1998).

[28] M. Visbal and R. Gordnier, "A high-order flow solver for deforming and moving meshes," AIAA Paper 2000-2619, 2000.

[29] A. Hashimoto, K. Murakami, T. Aoyama, R. Tagai, S. Koga, S. Nagai, and K. Hayashi, "Dynamic stability analysis of a reentry lifting capsule with detached eddy simulation," AIAA Paper 2016-0552, 2016.

[30] A. Hashimoto, K. Murakami, T. Aoyama, K. Yamamoto, M. Murayama, and P. R. Lahur, "Drag prediction on NASA common research model using automatic hexahedra grid-generation method," J. Aircr. **51**, 1172–1182 (2014).

[31] Y. Ohmichi, T. Ishida, and A. Hashimoto, "Modal decomposition analysis of three-dimensional transonic buffet phenomenon on a swept wing," AIAA J. **56**, 3938–3950 (2018).

[32] P. Holmes, J. L. Lumley, G. Berkooz, and C. W. Rowley, *Turbulence, Coherent Structures, Dynamical Systems and Symmetry*, 2nd ed. (Cambridge University Press, Cambridge, 2012).

[33] R. Arora, A. Cotter, K. Livescu, and N. Srebro, "Stochastic optimization for PCA and PLS," in *50th Annual Allerton Conference on Communication, Control, and Computing* (Allerton, 2012), pp. 861–868.

[34] J. L. Lumley, "The structure of inhomogeneous turbulent flows," in *Atmospheric Turbulence and Radio Propagation*, edited by A. M. Yaglom and V. I. Tatarski (Nauka, Moscow, 1967), pp. 166–178.

[35] M. R. Jovanović, P. J. Schmid, and J. W. Nichols, "Sparsity-promoting dynamic mode decomposition," Phys. Fluids **26**, 024103 (2014).

[36] R. Tibshirani, "Regression shrinkage and selection via the lasso," J. R. Stat. Soc.: Ser. B **58**, 267–288 (1994).

[37] E. Alenius, "Mode switching in a thick orifice jet, an LES and dynamic mode decomposition approach," Comput. Fluids **90**, 101–112 (2014).

[38] B. K. Natarajan, "Sparse approximate solutions to linear systems," SIAM J. Comput. **24**, 227–234 (1995).

[39] J. C. R. Hunt, A. Wray, and P. Moin, "Eddies, stream, and convergence zones in turbulent flows," Technical Report No. CTR-S88, Center for Turbulence Research Report, Stanford, 1988.

[40] P. Welch, "The use of fast Fourier transform for the estimation of power spectra: A method based on time averaging over short modified periodograms," IEEE Trans. Audio Electroacoust. **15**, 70–73 (1967).

[41] H. P. Pao and T. W. Kao, "Vortex structure in the wake of a sphere," Phys. Fluids **20**, 187–191 (1977).
[42] G. Constantinescu and K. Squires, "Numerical investigations of flow over a sphere in the subcritical and supercritical regimes," Phys. Fluids **16**, 1449–1466 (2004).
[43] G. Yun, D. Kim, and H. Choi, "Vortical structures behind a sphere at subcritical Reynolds numbers," Phys. Fluids **18**, 015102 (2006).
[44] O. Marquet and M. Larsson, "Global wake instabilities of low aspect-ratio flat-plates," Eur. J. Mech.: B/Fluids **49**, 400–412 (2015).
[45] D. Sujudi and R. Haimes, "Identification of swirling flow in 3-D vector fields," AIAA Paper No. 95-1715, 1995.
[46] I. Rodriguez, R. Borell, O. Lehmkuhl, and C. D. P. Segarra, "Direct numerical simulation of the flow over a sphere at Re = 3700," J. Fluid Mech. **679**, 263–287 (2011).
[47] K. Mitsuo, H. Iijima, Y. Aoki, M. Kohzai, K. Nakakita, S. Nagai, K. Fujii, K. Murakami, and E. Nakano, "HTV-R recovery capsule wind tunnel tests in transonic and supersonic speeds," in *56th Proceedings of the Space Sciences and Technology Conference* (The Japan Society for Aeronautical and Space Sciences, 2012), pp. JSASS–2012–4640.